Vietnam Journal of Catalysis and Adsorption
Tạp chí xúc tác và hấp phụ Việt Nam

https://jca.edu.vn

Chelation-assisted synthesis and magnetic properties of functionalized Graphene-Fe_3O_4 hybrids

Bui Hung Thang[2], Phan Ngoc Minh[3], To Anh Duc[1,*]

[1] *Vietnam National Space Center, Vietnam Academy of Science and Technology, 18 Hoang Quoc Viet, Hanoi, Vietnam*
[2] *Institute of Materials Science, Vietnam Academy of Science and Technology, 18 Hoang Quoc Viet, Hanoi, Vietnam*
[3] *Graduate University of Science and Technology, Vietnam Academy of Science and Technology, 18 Hoang Quoc Viet, Hanoi, Vietnam*
** Email: taduc@vnsc.org.vn*

ARTICLE INFO

Received: 08/01/2026
Accepted: 13/02/2026
Published: 30/03/2026

Keywords:
Graphene–COOH;
Fe_3O_4 nanoparticles;
electromagnetic absorption;
interfacial polarization;
soft ferrimagnetism

ABSTRACT

Carboxyl-functionalized graphene–Fe_3O_4 hybrids were synthesized via oxidative treatment of graphene nanoplatelets followed by chelation-assisted in situ coprecipitation of magnetite. Spectroscopic and microscopic analyses confirmed the successful introduction of –COOH groups and their role as multidentate ligands, directing the uniform nucleation of nanocrystalline Fe_3O_4 on crumpled graphene sheets. The resulting hierarchical, porous architecture provides intimate interfacial contact between the conductive graphene framework and the magnetic phase, thereby favouring multiple internal reflections, interfacial polarization and synergistic conductive, dipolar and space-charge loss mechanisms. Magnetic measurements demonstrated soft ferrimagnetic behaviour with high saturation magnetization and low coercivity and remanence, a combination desirable for high-frequency absorber applications due to efficient dynamic magnetic loss with limited hysteretic and eddy-current dissipation. These findings establish a clear processing–structure–property relationship and highlight Graphene–COOH/Fe_3O_4 hybrids as promising candidates for lightweight, broadband electromagnetic-absorbing coatings suitable for advanced stealth and electromagnetic protection of high-speed aerial platforms.

Introduction

Electromagnetic wave absorption has become a critical design requirement for modern flying platforms such as missiles and unmanned aerial vehicles, which increasingly operate in dense, multi-band surveillance and tracking environments [1-10]. Conventional strategies for radar cross-section reduction often rely on purely geometric shaping or on coatings that predominantly reflect incident electromagnetic energy, approaches that can be insufficient against advanced, multi-frequency detection systems and can introduce significant aerodynamic or structural penalties. In contrast, materials that can efficiently dissipate incident electromagnetic energy within a thin, lightweight coating offer a more elegant pathway to electromagnetic signature management [11-20]. For high-speed aerial vehicles, such absorbers must simultaneously exhibit low density, robust mechanical and thermal stability, and broadband attenuation

https://doi.org/10.62239/jca.2026.002

under varying angles of incidence and operational conditions. These stringent constraints have stimulated intensive research into advanced nanostructured absorbers, especially those that can couple dielectric and magnetic loss mechanisms in a controllable manner, thereby enabling high-performance, application-oriented electromagnetic absorption layers for stealth and survivability of flying objects [21-30].

Within this context, functionalized graphene–Fe_3O_4 hybrid systems emerge as a particularly promising class of candidates, as they combine the high electrical conductivity, large specific surface area, and tunable dielectric response of graphene with the strong magnetic loss and permeability characteristics of Fe_3O_4 nanoparticles. Chemical functionalization of the graphene phase enhances dispersion, interfacial bonding, and defect-mediated polarization, while the incorporation of Fe_3O_4 introduces multiple magnetic resonance pathways and improves impedance matching between free space and the absorber layer. The resulting hybrid architecture can, in principle, provide synergistic dielectric–magnetic loss, enlarged interfacial polarization, and increased multiple scattering of electromagnetic waves, all of which are desirable for efficient attenuation within a limited thickness. In the present work, we therefore aim to fabricate functionalized graphene–Fe_3O_4 hybrid materials and to systematically investigate their structural, magnetic, and dielectric characteristics, together with their electromagnetic absorption behavior in the relevant microwave regime. The specific objective of this study is to establish a clear processing–structure–property relationship for these hybrids and to assess their suitability as lightweight, high-efficiency electromagnetic absorbing media for potential application in protective coatings on missiles and drone platforms.

Experimental

In this work, carboxylated graphene (Graphene–COOH, denoted Gr-COOH) is obtained by chemically functionalizing commercial graphene nanoplatelets (GNPs) through oxidative treatment in a mixed strong-acid medium. The starting GNPs possess high purity (99.5%), a thickness in the range of 2–10 nm and an average lateral size of about 5 µm, providing a large accessible surface area for chemical modification. The surface functionalization is carried out using a mixture of concentrated nitric acid (HNO_3) and sulfuric acid (H_2SO_4), which acts as a powerful oxidizing system capable of attacking the sp^2-bonded carbon network at defect sites and sheet edges. Under these oxidative conditions, the π-conjugated lattice is partially disrupted, creating defects and opening sites for oxygen-containing groups to be grafted onto the graphene surface; in particular, carboxyl (–COOH) moieties are anchored at newly formed edge and defect sites. The structural evolution induced by the acid treatment is evidenced by Raman spectroscopy (Figure 1a). A pronounced D band appears at around 1340 cm^{-1} in Gr–COOH, and the corresponding intensity ratio I_D/I_G=0.42, indicating an increased defect density and partial conversion of sp^2 (C=C) domains into sp^3-disrupted (C–C) regions associated with oxidative functionalization. In addition, the 2D (G′) band (≈2700 cm^{-1}) is a second-order double-resonance feature that does not require defects for activation; its intensity and profile are sensitive to electronic coherence and stacking order. The comparatively weaker/broader 2D response after functionalization is consistent with disruption of the π-conjugated network by edge/defect functional groups introduced during acid treatment.

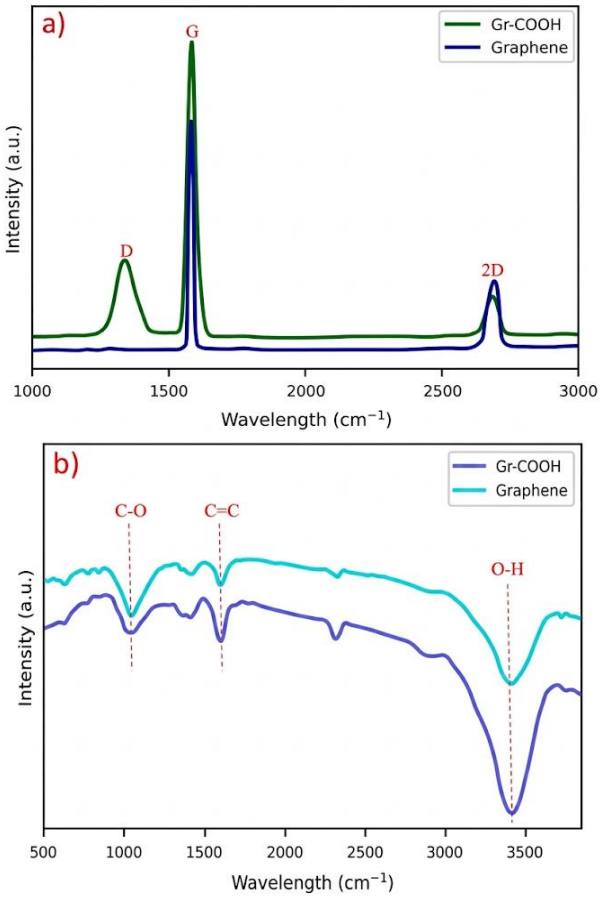

Figure 1. Spectroscopic characterization of Gr–COOH: (a) Raman spectrum; (b) FTIR spectrum

Complementary FTIR analysis (Figure 1b) further confirms the successful introduction of carboxyl

groups: in addition to the broad O–H stretching band, the functionalized material exhibits a clear C=O stretching peak near 1708 cm^{-1} associated with –COOH groups, together with C–O related vibrations, demonstrating that the mixed HNO_3/H_2SO_4 treatment has effectively grafted carboxyl functionalities onto the graphene nanoplatelet surface and yielded the desired Gr-COOH precursor for subsequent processing.

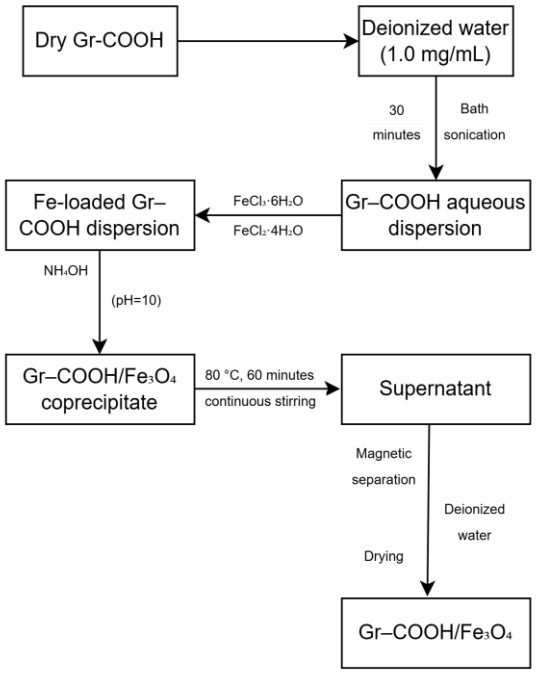

Figure 2. Schematic illustration of the synthesis route for the Graphene–COOH/Fe_3O_4 hybrid

Building on the previously obtained carboxylated graphene (Gr–COOH), a chelation-assisted in situ coprecipitation route was employed to synthesize the Graphene–COOH/Fe_3O_4 hybrid. Dried Gr–COOH powder was first redispersed in deionized water at a concentration of approximately 1.0 mg mL^{-1} and sonicated in a bath for 30 min to afford a stable, uniformly dark suspension of exfoliated nanoplatelets. Subsequently, $FeCl_3·6H_2O$ and $FeCl_2·4H_2O$ were dissolved directly into this dispersion in a Fe^{3+}:Fe^{2+} molar ratio of 2:1 under vigorous mechanical stirring (600–800 rpm). Aqueous NH_4OH was then added dropwise until the pH reached about 10, at which point the carboxyl groups on Gr–COOH became predominantly deprotonated to $–COO^-$ and acted as multidentate coordination sites for Fe^{2+}/Fe^{3+} ions. This immediate chelation of iron species at graphene edges and defect regions biases the subsequent nucleation and growth of magnetite toward the Gr–COOH surface, favoring intimate interfacial bonding rather than free particle formation in the bulk solution. The reaction mixture was heated to 80 °C and maintained at this temperature for 60 min under continuous stirring to allow complete formation of Fe_3O_4 nanocrystals anchored on the graphene framework via the classical coprecipitation pathway. After cooling to room temperature, the black magnetic product was separated from the supernatant using a permanent magnet, repeatedly washed with deionized water to remove residual ions and unbound species, and finally dried in an air oven at 50 °C to yield a free-flowing Graphene–COOH/Fe_3O_4 hybrid powder suitable for subsequent structural, magnetic, dielectric, and electromagnetic absorption characterization.

Results and discussion

The TEM micrographs in Figure 3a and 3b provide clear visual evidence of the successful formation of the Graphene–COOH/Fe_3O_4 hybrid with nanoscale magnetite domains intimately anchored to the functionalized graphene scaffold.

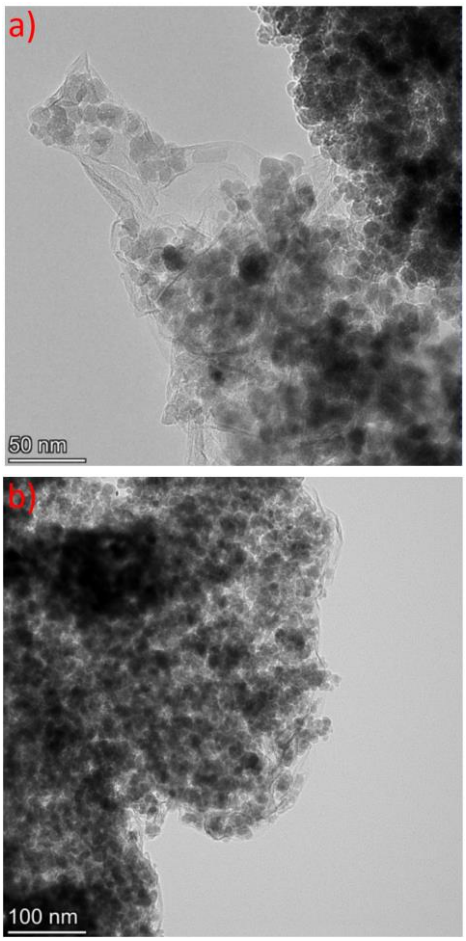

Figure 3. TEM images of Graphene–COOH/Fe_3O_4 hybrid at different magnifications: a) lower-magnification overview; b) higher-magnification view highlighting nanoparticle decoration

https://doi.org/10.62239/jca.2026.002

In Figure 3a, the underlying graphene–COOH appears as a semi-transparent, wrinkled sheet extending from the left-hand side of the frame, while numerous dark, nearly spherical nanoparticles with sizes on the order of a few to several tens of nanometres are uniformly decorating its surface and edges. This contrast pattern is fully consistent with Fe_3O_4 nanocrystals nucleated directly on a low-Z carbon support: the graphene layers are thin enough to be electron-transparent, whereas the higher-Z iron oxide phase gives rise to strongly absorbing, dark features. The absence of large, free-standing Fe_3O_4 aggregates in the surrounding region, together with the dense coverage of the sheet, suggests that the chelation-driven coprecipitation indeed biased nucleation to the carboxylated graphene interface, generating a high density of well-dispersed nanocrystals anchored via –COO^-–Fe linkages. Figure 3b shows a thicker, more three-dimensional cluster in which the dark Fe_3O_4 nanoparticles form a continuous, sponge-like ensemble that still appears to be supported by or intertwined with graphene lamellae at the periphery. The roughly uniform nanoparticle contrast and the absence of micron-scale domains point to controlled growth and limited Ostwald ripening, despite the omission of external capping agents. Together, these micrographs indicate that the proposed synthesis yields a hierarchical hybrid architecture: crumpled graphene–COOH sheets act as flexible two-dimensional templates, densely coated with nanocrystalline Fe_3O_4, which can interconnect into larger secondary agglomerates while retaining nanoscale porosity. Such a morphology: high interfacial area, intimate dielectric–magnetic contact, and a percolated network of magnetite domains, is expected to be particularly favourable for electromagnetic wave attenuation, as it facilitates multiple scattering, interfacial polarization, and efficient magnetic loss within a relatively thin absorber layer.

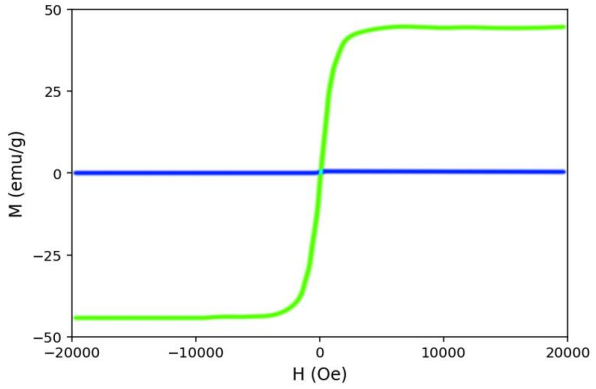

Figure 4. Magnetic hysteresis (M–H) curve of the Gr–COOH/Fe_3O_4 hybrid

Figure 4 presents the room-temperature magnetic hysteresis (M–H) curve of the Graphene–COOH/Fe_3O_4 hybrid, measured in the field range −20 kOe to +20 kOe. The loop exhibits a steep sigmoidal increase of magnetization around zero field and rapid approach to a well-defined saturation plateau at high fields, characteristic of a soft ferrimagnetic response dominated by the Fe_3O_4 phase. The essentially horizontal high-field segments indicate that the magnetization of the hybrid is fully aligned within the accessible field window, confirming that the Fe_3O_4 nanocrystals retain their intrinsic ferrimagnetic ordering after anchoring onto the Gr–COOH framework. In contrast, the Gr–COOH reference sample shows an almost field-independent magnetization close to zero (blue baseline in the plot), confirming that the graphene component is magnetically inert and that the observed response originates from the magnetite nanoparticles intimately bound to the functionalized graphene sheets. This pronounced saturation behavior demonstrates that the hybrid can provide robust magnetic loss channels, which are essential for effective dissipation of the magnetic component of incident electromagnetic waves in absorber applications.

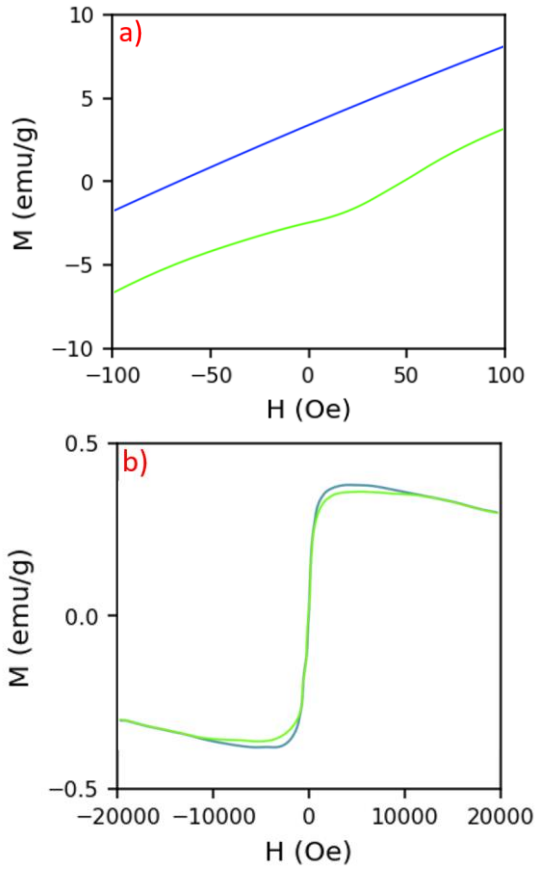

Figure 5: a) Enlarged low-field M–H curve of the Gr–COOH/Fe_3O_4 hybrid; b) Normalized M–H hysteresis loop of the Gr–COOH/Fe_3O_4 hybrid

https://doi.org/10.62239/jca.2026.002

Figure 5a shows an enlarged view of the low-field region of the M–H curve, allowing the coercive field and remanent magnetization to be resolved with higher precision. In this magnified window (−100 to +100 Oe), the hysteresis loop is extremely narrow and only weakly open, with magnetization crossing the origin almost linearly and remanence remaining very close to zero. This low-hysteresis, near-reversible response is broadly consistent with prior reports on graphene-supported Fe_3O_4 nanocrystal hybrids, where nanoscale magnetic domains combined with a nonmagnetic carbon scaffold typically suppress strong interparticle coupling and domain-wall pinning, resulting in low coercivity and negligible remanence. In comparison to more strongly interacting Fe_3O_4 aggregates that commonly exhibit a more open loop, the present hybrid benefits from ligand-guided nucleation and anchoring on the functionalized graphene surface, which promotes dispersion and magnetic decoupling through interfacial separation. This literature-consistent trend supports our interpretation that the observed soft-magnetic behavior originates from the controlled nanoparticle distribution enforced by the Gr–COOH framework and is favorable for high-frequency applications due to reduced macroscopic hysteretic losses.

To make the demagnetization behavior explicit, we note that the coercive field (Hc) and remanent magnetization (Mr), or equivalently the remanence ratio (Mr/Ms), are very small for the hybrid, as evidenced by the extremely narrow low-field loop. This soft-magnetic response is in line with prior reports on graphene-supported Fe_3O_4 nanocrystals, where nanoscale dispersion typically yields low hysteresis while the non-magnetic carbon component reduces the mass-normalized magnetization compared with bulk Fe_3O_4. Such a profile is typical of a soft magnetic or quasi-superparamagnetic ensemble of Fe_3O_4 nanocrystals, in which thermal fluctuations and interfacial pinning strongly suppress domain wall pinning and irreversible switching. The small coercivity indicates that the nanoparticles are magnetically decoupled to a significant extent, which is consistent with their dispersion on the Gr–COOH surface and the presence of nonmagnetic graphene spacers between individual grains. This soft magnetic character is particularly advantageous for high-frequency operation, as it minimizes energy loss from macroscopic hysteresis while still enabling substantial dynamic susceptibility and magnetic resonance within the GHz regime.

Figure 5b displays the normalized M–H hysteresis loop of the hybrid, in which the magnetization axis has been scaled to highlight the subtle features of the magnetization process. In this representation, the central region of the curve appears nearly linear and reversible, while the loop opening remains extremely small over the entire −20 kOe to +20 kOe range. The normalized plot underscores that the dominant contribution of the Fe_3O_4 phase is a reversible rotation and alignment of nanocrystal magnetic moments in response to the applied field, rather than large-scale domain wall motion accompanied by pronounced hysteresis. The combination of a steep initial slope (high initial susceptibility), rapid saturation, and negligible normalized remanence confirms that the Gr–COOH/Fe_3O_4 hybrid behaves as a soft ferrimagnetic system with efficient field-induced magnetization dynamics.

Taken together, Figures 4 and 5 demonstrate that the Graphene–COOH/Fe_3O_4 hybrid possesses a high saturation magnetization provided by the Fe_3O_4 nanophase, yet retains very low coercivity and remanence owing to the nanoscale dispersion and interfacial separation enforced by the Gr–COOH scaffold. This combination of strong magnetic response and soft magnetic behavior is ideal for microwave-absorbing materials, as it enables intense magnetic loss through rapid magnetization relaxation while avoiding large hysteretic losses and eddy-current-dominated behavior. The magnetic characteristics revealed in Figures 4 to 5 therefore corroborate the structural evidence from TEM and support the suitability of the synthesized hybrid as a promising dielectric–magnetic absorber for electromagnetic stealth applications.

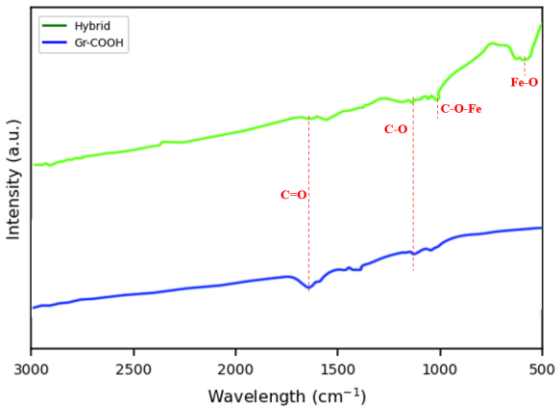

Figure 6. FTIR spectra of Gr–COOH and the Gr–COOH/Fe_3O_4 hybrid

The FTIR spectra in Figure 6 provide spectroscopic evidence for oxidative functionalization of the graphene precursor and for subsequent chemical

https://doi.org/10.62239/jca.2026.002

interaction during hybrid formation. For the Gr–COOH precursor, the presence of oxygenated functionalities is confirmed by a pronounced carbonyl band (C=O) near 1708 cm^{-1} associated with carboxyl groups, together with broad O–H stretching and C–O-related bands [31]. Although the overall FTIR envelope of graphene-based powders may appear only subtly altered after oxidation, because the sp^2 carbon framework is inherently weak in IR absorption [32] and the newly introduced polar groups are concentrated mainly at sheet edges and defect regions [33] rather than uniformly across the basal plane, the emergence of these O–H/C–O/C=O signatures provides direct evidence of successful functionalization. Upon hybrid formation, the spectrum of the Gr–COOH/Fe_3O_4 composite displays a noticeable reduction in the intensity of the C=O and O–H features, accompanied by slight peak shifts, indicating coordination of Fe^{2+}/Fe^{3+} ions with the deprotonated carboxylate groups (–COO^-) during coprecipitation. This interfacial metal–carboxylate bonding is essential for stabilizing Fe_3O_4 nucleation on the graphene surface, and the observed spectral evolution is fully consistent with chelation-driven magnetite growth. In the lower-wavenumber region (below ~600 cm^{-1}), the hybrid exhibits distinctive Fe–O lattice vibrations attributed to the stretching modes of the Fe_3O_4 spinel structure, further confirming the formation of crystalline magnetite within the composite. Overall, the FTIR signatures in Figure 6 corroborate the successful chemical integration of Fe_3O_4 nanocrystals with Gr–COOH and provide molecular-level evidence for the strong interfacial coupling that underpins the hybrid's enhanced dielectric–magnetic response and its suitability for electromagnetic absorption applications.

Conclusion

In this study, carboxyl-functionalized graphene–Fe_3O_4 hybrids were synthesized via oxidative functionalization of graphene nanoplatelets followed by chelation-assisted in situ coprecipitation, providing a simple route to interfacial control. Structural and spectroscopic results show that –COOH groups act as coordination ligands, regulating Fe_3O_4 nucleation and yielding crumpled graphene sheets uniformly decorated with nanocrystalline magnetite, i.e., a hierarchical porous hybrid with intimate graphene/Fe_3O_4 contact. A key finding is that this ligand-guided architecture simultaneously delivers soft-ferrimagnetic behavior (high saturation magnetization with very low coercivity and remanence) and an interface-rich microstructure that can support interfacial polarization and multi-reflection attenuation, making the hybrid a credible lightweight platform for electromagnetic-attenuating coatings.

Future work will focus on performance consolidation and deployment: tuning Fe_3O_4 loading/particle size and functional-group density, measuring complex permittivity–permeability and reflection loss for impedance matching, and validating durability, adhesion, and environmental stability after incorporation into practical coating matrices on metallic substrates.

Acknowledgments

This research is funded by Vietnam Academy of Science and Technology (VAST) under grant number NCPTVL.02/25-27.

References

1. Z. Wei, Z. Li, D. Chen, J. Liang, J. Kong, Small Struct., 6(7) (2025) 2400615. https://doi.org/10.1002/sstr.202400615
2. R. Che, J. Gu, J. Kong, W. Lu, Y. Huang, H. Lv, J. Liu, H. Wu, Cell Rep. Phys. Sci., 6(3) (2025) 102502. https://doi.org/10.1016/j.xcrp.2025.102502
3. S. Zhang, J. Zheng, Z. Zhao, S. Du, D. Lan, Z. Gao, G. Wu, Adv. Funct. Mater., (2025) e13762. https://doi.org/10.1002/adfm.202513762
4. Q. Chen, Y. Wang, Y. Xiong, H. Hu, N. Meng, Y. Liao, Adv. Fiber Mater., (2025) 1–30. https://doi.org/10.1007/s42765-025-00522-z
5. H. Peng, D. Zhang, Z. Xie, S. Lu, Y. Liu, F. Liang, Small, 21(8) (2025) 2408570. https://doi.org/10.1002/smll.202408570
6. X. Zhang, G. Xin, N. Wu, F. Pan, J. Liu, Z. Zeng, Research, 8 (2025) 0876. https://doi.org/10.34133/research.0876
7. G. Chen, Z. Li, L. Zhang, Q. Chang, X. Chen, X. Fan, J. Liu, H. Wu, Cell Rep. Phys. Sci., 5(7) (2024) 102097. https://doi.org/10.1016/j.xcrp.2024.102097
8. K. Cao, W. Ye, Y. Zhang, L. Shen, R. Zhao, W. Xue, X. Yang, J. Mater. Sci. Technol., 195 (2024) 63–73. https://doi.org/10.1016/j.jmst.2023.12.069
9. X.C. Zhang, M. Zhang, M.Q. Wang, L. Chang, L. Li, M.S. Cao, Adv. Funct. Mater., 34(44) (2024) 2405972. https://doi.org/10.1002/adfm.202405972
10. C. Liu, J. Lin, N. Wu, C. Weng, M. Han, W. Liu, Z. Zeng, Carbon, 223 (2024) 119017. https://doi.org/10.1016/j.carbon.2024.119017

11. L. Xia, T. Lu, M. Kong, J. Pei, Y. Huang, Y. Niu, G. Li, Prog. Org. Coat., 198 (2025) 108938. https://doi.org/10.1016/j.porgcoat.2024.108938
12. Q. Wang, Y. Liu, Y. Ma, E. Su, X. Su, J. Alloys Compd., 1021 (2025) 179666. https://doi.org/10.1016/j.jallcom.2025.179666
13. F. Zhang, L. Wu, H. Su, J. Jiang, J. Tian, K. Sun, R. Fan, Ceram. Int., 51(6) (2025) 7026–7037. https://doi.org/10.1016/j.ceramint.2024.12.137
14. Y. Li, W. Zhang, T. Chen, L. Ma, F. Liu, E.H. Han, J. Colloid Interface Sci., 683 (2025) 1–15. https://doi.org/10.1016/j.jcis.2024.12.153
15. H. Li, K. Li, X. Zhou, Mater. Lett., (2025) 138691. https://doi.org/10.1016/j.matlet.2025.138691
16. S. Mu, S. Wang, X. Pang, J. Pu, J. Alloys Compd., 975 (2024) 172956. https://doi.org/10.1016/j.jallcom.2023.172956
17. J. Zhu, D. Lan, X. Liu, S. Zhang, Z. Jia, G. Wu, Small, 20(47) (2024) 2403689. https://doi.org/10.1002/smll.202403689
18. Q. Wu, W. Li, X. Yan, Coatings, 13(9) (2023) 1478. https://doi.org/10.3390/coatings13091478
19. P. Huang, X. Niu, Y. Wang, B. Zou, J. Am. Ceram. Soc., 106(10) (2023) 5832–5845. https://doi.org/10.1111/jace.19201
20. L. Xia, K. Wang, W. Xu, M. Kong, Y. Huang, Y. Lv, G. Li, Prog. Org. Coat., 182 (2023) 107686. https://doi.org/10.1016/j.porgcoat.2023.107686
21. H. Jin, M. Liu, L. Wang, W. You, K. Pei, H.W. Cheng, R. Che, Natl. Sci. Rev., 12(2) (2025) nwae420. https://doi.org/10.1093/nsr/nwae420
22. J. Brdarić Kosanović, B. Marković, I. Miličević, A. Stanković, D. Tatar, Crystals, 15(11) (2025) 959. https://doi.org/10.3390/cryst15110959
23. T. Wu, S. Bi, H. Li, R. Xing, J. Yang, X. Liu, Z. Li, Discover Nano, 20(1) (2025) 107. https://doi.org/10.1186/s11671-025-04287-7
24. S.H. Siddiki, C.K. Maity, S. Sahoo, J. Mater. Chem. A, 13(38) (2025) 31869–31920. https://doi.org/10.1039/D5TA03936C
25. P. Kumar, A. Kumar, ACS Appl. Nano Mater., (2025). https://doi.org/10.1021/acsanm.5c02368
26. Y. Chen, Z.Y. Zhang, X.Q. Yin, F. Zhang, Russ. J. Phys. Chem. B, 19(1) (2025) 171–192. https://doi.org/10.1134/S1990793124701641
27. X. Zhang, X. Zhang, D. Liu, L. Wang, G. Wen, Y. Wang, X. Huang, Langmuir, 40(36) (2024) 18857–18881. https://doi.org/10.1021/acs.langmuir.4c02829
28. T. Zhao, F. Ye, B. Huang, Z. Li, L. Cheng, ACS Appl. Mater. Interfaces, 16(39) (2024) 51860–51875. https://doi.org/10.1021/acsami.4c09772
29. H. Cai, J. Guo, H. Hu, Y. Liu, M. Jia, H. Chen, G. Zhou, ACS Appl. Nano Mater., 7(10) (2024) 11302–11312. https://doi.org/10.1021/acsanm.4c00827
30. C. Wu, Y. Liu, G. Zhao, ACS Appl. Nano Mater., 7(8) (2024) 8926–8938. https://doi.org/10.1021/acsanm.4c00438
31. D. Khalili, New J. Chem., 40(3) (2016) 2547–2553. https://doi.org/10.1039/C5NJ02314A
32. N.A. Rangel-Vázquez, A. Bonilla-Petriciolet, E.A. Márquez-Brazón, Y. Huerta, R. Zavala-Arce, J.D. Rodríguez-Macías, Nanomaterials, 15(16) (2025) 1234. https://doi.org/10.3390/nano15161234
33. A. Lerf, H. He, M. Forster, J. Klinowski, J. Phys. Chem. B, 102(23) (1998) 4477–4482. https://doi.org/10.1021/jp9731821